This is the accepted version of the publication Li L, Faisal Haider M, Mei H, Giurgiutiu V, Xia Y. Theoretical calculation of circular-crested Lamb wave field in single- and multi-layer isotropic plates using the normal mode expansion method. Structural Health Monitoring. 2020;19(2):357-372.
 DOI: 10.1177/1475921719848149

Theoretical calculation of circular-crested Lamb wave field in single- and multi-layer isotropic plates using normal mode expansion method

Lingfang Li[1], Mohammad Faisal Haider[2], Hanfei Mei[3], Victor Giurgiutiu[4], Yong Xia[5]

[1] PhD candidate, Department of Civil and Environmental Engineering, The Hong Kong Polytechnic University, Hung Hom, Kowloon, Hong Kong. Email: lingfang.li@connect.polyu.hk;

[2] Graduate Research Assistant, Department of Mechanical Engineering, University of South Carolina, Columbia, SC, USA. Email: haiderm@email.sc.edu;

[3] PhD candidate, Department of Mechanical Engineering, University of South Carolina, Columbia, SC, USA. Email: hmei@email.sc.edu;

[4] Professor, Department of Mechanical Engineering, University of South Carolina, Columbia, SC, USA. Email: victorg@mailbox.sc.edu;

[5] Corresponding author: Professor, Department of Civil and Environmental Engineering, The Hong Kong Polytechnic University, Hung Hom, Kowloon, Hong Kong. Email: y.xia@polyu.edu.hk.

Abstract

The guided wave technique is commonly used in the health monitoring of thin walled structures because the guided waves can propagate far in the structures without much energy loss. However, understanding of the wave propagation in bounded layered structures is still lacking. In this study, the Lamb wave field of single- and multi-layer plates excited by surface-mounted piezoelectric wafer active sensors is theoretically analyzed using normal mode expansion (NME) method, which is based on the elastodynamic reciprocity relation and utilizes the orthogonality relations of the Lamb wave modes. The mode participation factors of Lamb wave in single- and multi-layer isotropic plates are derived. The time domain responses are obtained through the inverse Fourier transform of the structural response spectrum, which is obtained by multiplying the transfer function with the excitation frequency spectrum. The developed NME method is first applied to an aluminum single-layer plate. The obtained analytical tuning curves and out-of-plane velocity of the plate are in good agreement with the numerical and experimental results. Finally the analytical wave responses of an aluminum-adhesive-steel triple-layer plate are verified through comparison with the finite element analysis and experiment. The proposed NME method provides a reliable and accurate calculation of the wave field in single- and multi-layer plates.

Keywords: Lamb wave, isotropic plates, piezoelectric wafer active sensor (PWAS), normal mode expansion (NME), elastodynamic reciprocity relation, tuning curve

1 Introduction

The guided wave technology[1], which uses ultrasonic waves that can propagate far in the waveguide without much energy loss, is suitable for inspecting large areas of complicated structures and has gained wide attention from structural health monitoring (SHM) communities in recent decades. Guided waves are commonly excited by directly attached electromagnetic-acoustic transducers[2, 3] and piezoelectric transducers[4]. Piezoelectric wafer active sensors (PWASs) are commonly used to generate and receive guided waves in SHM applications due to the direct and converse piezoelectric effects[5]. Contrary to conventional transducers, PWASs are low cost, lightweight, and unobtrusive to the monitored structures. They can be permanently bonded to the host structures in large quantities and achieve real-time SHM. PWASs can be used in various modes, including pitch-catch, pulse echo, phased array, and electromechanical impedance modes[6]. Possible structural damage such as delamination, debonding, dents, and cracks, which change the waveguide properties and introduce wave scatters, can be detected by examining the changes in the wave amplitudes and packet shapes and the newly emerged wave packets[7, 8].

In plate-like structures, the commonly used guided wave types include the Lamb and shear horizontal waves. Such waves are dispersive and contain multimode. Several efficient techniques have been developed to study the wave properties in plates, such as the global matrix method (GMM)[9, 10], transfer matrix method[11], stiffness matrix method[12], elastodynamic finite integration technique[13], spectral finite element method[14], and semi-analytical finite element (SAFE)[15, 16] method. These methods provide the stationary guided wave dispersion and mode shape information in the frequency domain.

The guided wave responses induced by transient excitations contain broad frequency contents due to their dispersive nature. They are analyzed in frequency domain first and then transferred back into the time domain. Several methods have been developed to calculate the plate frequency domain responses induced by various types of external excitations. For example, the wave fields induced by a point load (in normal or oblique directions) have been analytically and semi-analytically calculated by the Green's function[16, 17]. The line load-induced wave field of straight-crested wave can be obtained if the plane strain assumption is adopted. However, typically direct-bonded transmitters, such as circular or rectangular PWASs, have

finite dimensions. Thus, the loads cannot be assumed as point or line loads. The Lamb wave field amplitude induced by surface-mounted PWASs is commonly referred to as the Lamb wave tuning curve, which depends on the PWAS and plate properties and is related to the structural transfer function. In fact, this curve is equivalent to the transfer function if the excitation amplitude is 1, that is, unit excitation is applied.

The integral transform method (ITM)[18-20] has been used to obtain the tuning curves for straight- and circular-crested Lamb waves in single-layer isotropic plates. The ITM first transforms the wave governing equations for the straight-crested (or circular-crested) wave equations into the wavenumber domain through Fourier transform (or Hankel transform). The wavenumber domain solutions are then transferred back to the physical domain through the corresponding inverse transform. Complicated transform calculations are required among different domains in this method. Liu and Xi[21] incorporated ITM with numerical approximation in the plate thickness direction and proposed a hybrid numerical method to extend the ITM application to the composite plates. Barouni and Saravanos[22] studied the surface-excited straight-crested waves in lamina and sandwiched plates with the ITM.

The normal mode expansion (NME) method utilizes the orthogonality relations of Lamb wave modes to avoid the complicated transform calculations among domains. Only the stress and velocity mode shapes are required to obtain the tuning curves. With this method, Achenbach and Xu[23] predicted the wave field excited by a point source. Kamal *et al.*[24], Weaver and Pao[25], and Moulin *et al.*[26] derived the tuning curves for straight-crested Lamb waves in plates. Santoni[27] approximated the tuning curve for circular-crested waves (excited by circular PWAS) without considering the decrease in wave amplitude. Mei and Giurgiutiu[28] also predicted the wave field in an anisotropic single-layer plate using the NME method in a semi-analytical manner.

Although the analytical solution for the straight crested wave field is available, straight-crested waves are not common in practical SHM applications as they are actually a planar strain simplification of most real-life cases. Ideally only line loads of infinite covering scope in the second in-plane dimension other than the wave propagation direction can generate straight crested wave field, for example a PWAS of a large aspect ratio with the short edge aligned with the wave propagation direction. PWASs of limited dimensions are more practical in real-life SHM applications, among which the circular shaped sensors rather than other shaped ones are

more favorable due to simplicity of the generated wave field. Therefore, the study of the circular wave field is of more practical significance. Although previous works have obtained the circular-crested wave fields in single-layer plates analytically and in multi-layer plates semi-analytically, there has no analytical solutions of circular-crested Lamb wave field in bounded layered structures, such as multi-layer shell structures, dry cask storage canisters and bonded plates, excited by finite dimension external excitations. In this study, the NME method is developed to solve the guided wave field in single- and multi-layer structures subjected to the circular PWAS excitations. Guided wave field solutions in frequency and time domains in single- and multi-layer plates are verified numerically and experimentally. This paper provides a basis for understanding the nature of the Lamb wave propagation in multi-layer plates.

2 PWAS basis

Piezoelectric materials couple the mechanical and electrical fields through the direct and converse piezoelectric effects as[5]

$$S_{ij} = s_{ijkl}^{E} T_{kl} + d_{kij} E_k , \tag{1}$$

$$D_j = d_{jkl} T_{kl} + \varepsilon_{kl}^{T} E_k , \tag{2}$$

where S_{ij} is the mechanical strain, T_{kl} the mechanical stress, E_k the electrical field, D_j the electrical displacement, s_{ijkl}^{E} the mechanical compliance of the material at zero electrical field ($E=0$), d_{jkl} the piezoelectric coupling factor, and ε_{kl}^{T} the dielectric permittivity at zero mechanical stress field ($T=0$). In a surface-mounted PWAS configuration, the d_{31} piezoelectric coupling effect is used, that is, the out-of-plane electrical field E_3 in the PWAS induces the in-plane strain, which will be transferred to the host structure through the adhesive layer[6, 19] shown in Figure 1. The shear stress distribution in the structure is shown in Figure 1(b). It concentrates more near the PWAS border when the bonding layer is thinner. In the ideal case, the thickness of the bonding layer is neglected, which is referred to as the pin-force model shown in Figure 1(c). The equivalent effective stress of the pin-force model is given by

$$\tau(r) = a^2 \tau_a \frac{\delta(r-a)}{r}, \tag{3}$$

$$\tau_a = \frac{\psi}{\alpha+\psi} \frac{t_a}{a} E_a \varepsilon_{ISA} , \tag{4}$$

where δ is the Dirac delta function. $\psi=Et/E_at_a$ is the stiffness factor with E and E_a as the

Young's moduli of the plate and PWAS, respectively; and t and t_a as their thicknesses. $\varepsilon_{ISA}=-d_{31}V/t_a$ is the induced strain with d_{31} as the piezoelectric factor and V as the applied voltage, and factor α depends on the stress, strain, and displacement distribution across the thickness. Under low-frequency dynamic conditions, α takes the value of 4.

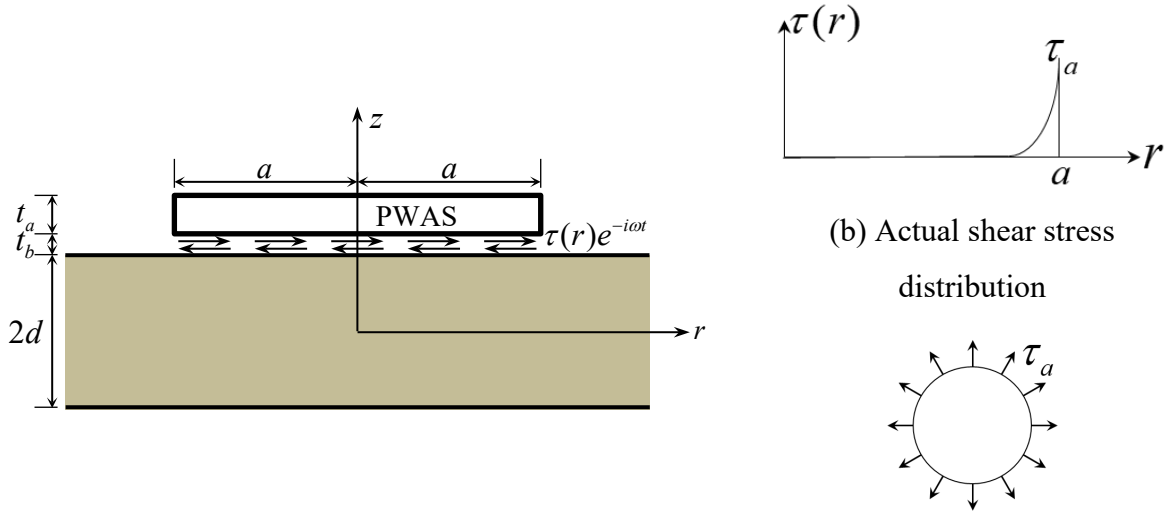

(a) Physical model

(b) Actual shear stress distribution

(c) Pin-force model

Figure 1 Interaction between the PWAS and host structure (t_a: PWAS thickness, a: radius of circular PWAS, t_b: bond layer thickness, d: half thickness of plate)

3 Theoretical background of NME

The NME method is based on the elastodynamic reciprocity relation and takes the advantages of the orthogonality relation of Lamb wave modes. This method can be used to find the amplitude of certain modes generated by external loads and evaluate the contribution of each mode to the total wave[29]. The NME method assumes that the actual wave field is the linear combination of wave modes with corresponding participation factors as

$$\boldsymbol{U}(r,\theta,t)=\sum_n a_n \boldsymbol{u}^n(r,\theta)e^{-i\omega t}, \tag{5}$$

$$\boldsymbol{T}(r,\theta,t)=\sum_n a_n \boldsymbol{\sigma}^n(r,\theta)e^{-i\omega t}, \tag{6}$$

where $\boldsymbol{U}(r, \theta, t)$ is the actual displacement vector that consists of $U_r(r, \theta, t)$, $U_\theta(r, \theta, t)$, and $U_z(r, \theta, t)$ components; and $\boldsymbol{T}(r, \theta, t)$ is the actual stress mode vector that consists of $T_{rr}(r, \theta, t)$, $T_{\theta\theta}(r,$

θ, t), $T_{zz}(r, \theta, t)$, $T_{\theta z}(r, \theta, t)$, $T_{rz}(r, \theta, t)$, and $T_{r\theta}(r, \theta, t)$ components. a_n is the participation factor of the n^{th} mode. Correspondingly, $\boldsymbol{u}^n(r, \theta)$ is the n^{th} displacement mode shape vector that consists of $u_r^n(r, \theta)$, $u_r^n(r, \theta)$, and $u_Z^n(r, \theta)$ components; and $\boldsymbol{\sigma}^n(r, \theta)$ is the n^{th} stress mode shape vector that consists of $\sigma_{rr}^n(r, \theta)$, $\sigma_{\theta\theta}^n(r, \theta)$, $\sigma_{zz}^n(r, \theta)$, $\sigma_{\theta z}^n(r, \theta)$, $\sigma_{rz}^n(r, \theta)$, and $\sigma_{r\theta}^n(r, \theta)$. Notably, the bold italic letters indicate that the term is a vector, and the normal italic letters indicate a scalar term. The wave fields in single- and multi-layer isotropic plates are investigated in this study, and the waves are independent of wave propagation direction θ. Equations (5) and (6) are then simplified as

$$\boldsymbol{U}(r,t) = \sum_n a_n \boldsymbol{u}^n \left(r\right) e^{-i\omega t}\,, \tag{7}$$

$$\boldsymbol{T}(r,t) = \sum_n a_n \boldsymbol{\sigma}^n \left(r\right) e^{-i\omega t}\,. \tag{8}$$

To calculate the wave field, the mode shapes and the participation factor are obtained as detailed in the following sections.

3.1 Lamb wave mode shape in plates

3.1.1 Lamb waves in single-layer plates

The Lamb wave fields have been studied by many researchers[6, 11, 30]. The governing equations for plate waves are

$$\frac{1}{r}\frac{\partial}{\partial r}\left(r\frac{\partial \Phi}{\partial r}\right)+\frac{\partial^2 \Phi}{\partial z^2}-\frac{1}{c_P^2}\ddot{\Phi}=0\,, \tag{9}$$

$$\frac{\partial}{\partial r}\left(\frac{1}{r}\frac{\partial (rH)}{\partial r}\right)+\frac{\partial^2 H}{\partial z^2}-\frac{1}{c_S^2}\ddot{H}=0\,, \tag{10}$$

where Φ and H are two potential functions; $c_P=\sqrt{(\lambda+2\mu)/\rho}$ and $c_S=\sqrt{\mu/\rho}$ are the pressure and shear wave speeds with λ and μ as the material Lame constants and ρ the density, respectively. The n^{th} wave mode shape components are

$$
\begin{aligned}
u_r^n &= -\left[\xi_n\left(A_1\sin\eta_{Pn}z + A_2\cos\eta_{Pn}z\right) + \eta_{Sn}\left(B_1\cos\eta_{Sn}z - B_2\sin\eta_{Sn}z\right)\right]H_1^{(1)}\left(\xi_n r\right)\\
u_z^n &= \left[\eta_{Pn}\left(A_1\cos\eta_{Pn}z - A_2\sin\eta_{Pn}z\right) + \xi_n\left(B_1\sin\eta_{Sn}z + B_2\cos\eta_{Sn}z\right)\right]H_0^{(1)}\left(\xi_n r\right)\\
\sigma_{rr}^n &= -\mu\left[\left(\xi_n^2 + \eta_{Sn}^2 - 2\eta_{Pn}^2\right)\left(A_1\sin\eta_{Pn}z + A_2\cos\eta_{Pn}z\right)\right.\\
&\quad \left. +2\xi_n\eta_{Sn}\left(B_1\cos\eta_{Sn}z - B_2\sin\eta_{Sn}z\right)\right]H_0^{(1)}\left(\xi_n r\right) - \frac{2\mu u_r^n}{r}\\
\sigma_{zz}^n &= \mu\left[\left(\xi_n^2 - \eta_{Sn}^2\right)\left(A_1\sin\eta_{Pn}z + A_2\cos\eta_{Pn}z\right) + 2\xi_n\eta_{Sn}\left(B_1\cos\eta_{Sn}z - B_2\sin\eta_{Sn}z\right)\right]H_0^{(1)}\left(\xi_n r\right)\\
\sigma_{rz}^n &= -\mu\left[2\xi_n\eta_{Pn}\left(A_1\cos\eta_{Pn}z - A_2\sin\eta_{Pn}z\right) + \left(\xi_n^2 - \eta_{Sn}^2\right)\left(B_1\sin\eta_{Sn}z + B_2\cos\eta_{Sn}z\right)z\right]H_1^{(1)}\left(\xi_n r\right)
\end{aligned}
\tag{11}
$$

where $\eta_{Pn}^2 = \omega^2/c_P^2 - \xi_n^2$ and $\eta_{Sn}^2 = \omega^2/c_S^2 - \xi_n^2$ with ξ_n as the n^{th} wavenumber. Parameters A_1, A_2, B_1, and B_2 can be determined from the boundary conditions, that is, the free surface traction condition. The first-type kind Hankel functions of order 0, $H_0^{(1)}$ and order 1, $H_1^{(1)}$, are used to indicate the outward propagation of the Lamb waves. The time dependency term $e^{-i\omega t}$ and other mode shape components not further used are not explicitly written hereafter, unless specified.

For simplicity in future expressions, the following notations are introduced, with the r and z components in Equation (11) replaced with x and y components to avoid possible confusions in the following derivations:

$$
\begin{aligned}
u_x^n &= i\xi_n\left(A_1\sin\eta_{Pn}y + A_2\cos\eta_{Pn}y\right) + i\eta_{Sn}\left(B_1\cos\eta_{Sn}y - B_2\sin\eta_{Sn}y\right)\\
u_y^n &= \eta_{Pn}\left(A_1\cos\eta_{Pn}y - A_2\sin\eta_{Pn}y\right) + \xi_n\left(B_1\sin\eta_{Sn}y + B_2\cos\eta_{Sn}y\right)\\
\sigma_{xx}^n &= -\mu\left[\left(\xi_n^2 + \eta_{Sn}^2 - 2\eta_{Pn}^2\right)\left(A_1\sin\eta_{Pn}y + A_2\cos\eta_{Pn}y\right) + 2\xi_n\eta_{Sn}\left(B_1\cos\eta_{Sn}y - B_2\sin\eta_{Sn}y\right)\right]\\
\sigma_{yy}^n &= \mu\left[\left(\xi_n^2 - \eta_{Sn}^2\right)\left(A_1\sin\eta_{Pn}y + A_2\cos\eta_{Pn}y\right) + 2\xi_n\eta_{Sn}\left(B_1\cos\eta_{Sn}y - B_2\sin\eta_{Sn}y\right)\right]\\
\sigma_{xy}^n &= i\mu\left[2\xi_n\eta_{Pn}\left(A_1\cos\eta_{Pn}y - A_2\sin\eta_{Pn}y\right) + \left(\xi_n^2 - \eta_{Sn}^2\right)\left(B_1\sin\eta_{Sn}y + B_2\cos\eta_{Sn}y\right)\right]
\end{aligned}
\tag{12}
$$

With these notations, Equation (11) is simplified as

$$
\begin{aligned}
u_r^n &= iu_x^n H_1^{(1)}\left(\xi_n r\right)\\
u_z^n &= u_y^n H_0^{(1)}\left(\xi_n r\right)\\
\sigma_{rr}^n &= \sigma_{xx}^n H_0^{(1)}\left(\xi_n r\right) + \frac{2\mu v_x^n H_1^{(1)}\left(\xi_n r\right)}{\omega r}\\
\sigma_{zz}^n &= \sigma_{yy}^n H_0^{(1)}\left(\xi_n r\right)\\
\sigma_{rz}^n &= i\sigma_{xy}^n H_1^{(1)}\left(\xi_n r\right)
\end{aligned}
\tag{13}
$$

The velocity mode shapes are then:

$$
\begin{aligned}
v_r^n &= iv_x^n H_1^{(1)}\left(\xi_n r\right) \\
v_z^n &= v_y^n H_0^{(1)}\left(\xi_n r\right)
\end{aligned}
\tag{14}
$$

3.1.2 Lamb waves in multi-layer plates

For a multi-layer plate, the dispersion curves could be obtained with the GMM. Take the double-layer plate in Figure 2 as an example, the boundary conditions include the free traction condition on the top and bottom surfaces and the traction and displacement continuity at the interface of the two layers:

$$
\begin{aligned}
&\text{Top surface:} && \boldsymbol{T}_1(z=d_1+d_2)=\{\mathbf{0}\} \\
&\text{Interface:} && \boldsymbol{T}_1(z=d_2)=\boldsymbol{T}_2(z=d_2) \\
& && \boldsymbol{U}_1(z=d_2)=\boldsymbol{U}_2(z=d_2) \\
&\text{Bottom surface} && \boldsymbol{T}_2(z=0)=\{\mathbf{0}\}
\end{aligned}
\tag{15}
$$

Equation (15) can be rewritten into the matrix form. The obtained square matrix that incorporates the displacement and stress states of all layers is called the "global matrix". Solving Equation (15) will result in the frequency-wavenumber dispersion curve of these multi-layer plate and from which the stress and displacement mode shapes can also be obtained.

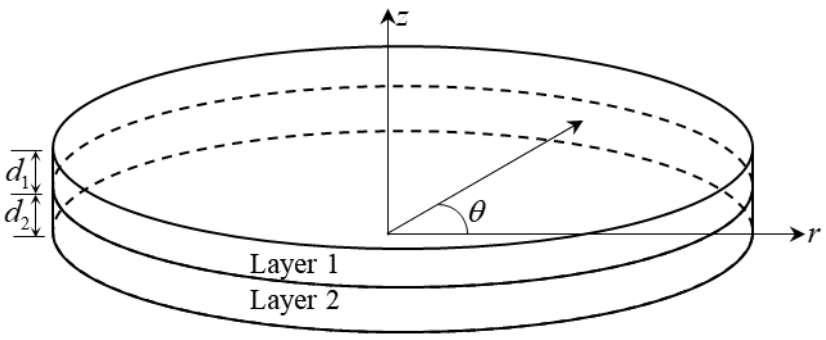

Figure 2 Schematic configuration of a double-layer plate

3.2 Reciprocity relation

Assuming $\boldsymbol{U}_{12}$ is the displacement at point 1 due to force $\boldsymbol{F}_2$ at point 2 and $\boldsymbol{U}_{21}$ is the

displacement at point 2 due to force $\boldsymbol{F}_1$ at point 1, then the reciprocity relation states that the work done by $\boldsymbol{F}_1$ upon displacement $\boldsymbol{U}_{12}$ equals the work by $\boldsymbol{F}_2$ upon $\boldsymbol{U}_{21}$[27], that is,

$$\boldsymbol{F}_1 \cdot \boldsymbol{U}_{12} = \boldsymbol{F}_2 \cdot \boldsymbol{U}_{21}. \tag{16}$$

The two forces generate velocity fields $\boldsymbol{V}_1$ and $\boldsymbol{V}_2$ and stress fields $\boldsymbol{T}_1$ and $\boldsymbol{T}_2$. Then, the complex reciprocity relation[31] is

$$\nabla(\tilde{\boldsymbol{V}}_2 \cdot \boldsymbol{T}_1 + \boldsymbol{V}_1 \cdot \tilde{\boldsymbol{T}}_2) = -(\tilde{\boldsymbol{V}}_2 \cdot \boldsymbol{F}_1 + \boldsymbol{V}_1 \cdot \tilde{\boldsymbol{F}}_2), \tag{17}$$

where the overhead tilde "~" stands for the complex conjugate of the corresponding term. For the circular-crested waves in cylindrical coordinate system, the complex reciprocity relation becomes

$$\begin{aligned} &\frac{1}{r}\frac{\partial}{\partial r}\left[r\left(\tilde{V}_r^2 T_{rr}^1 + V_r^1 \tilde{T}_{rr}^2 + \tilde{V}_z^2 T_{rz}^1 + V_z^1 \tilde{T}_{rz}^2\right)\right] + \frac{\partial}{\partial z}\left(V_z^1 \tilde{T}_{zz}^2 + \tilde{V}_z^2 T_{zz}^1 + V_r^1 \tilde{T}_{rz}^2 + \tilde{V}_r^2 T_{rz}^1\right) \\ &= -\left(\tilde{V}_r^2 F_r^1 + V_r^1 F_r^2 + \tilde{V}_z^2 F_z^1 + V_z^1 F_z^2\right) \end{aligned}, \tag{18}$$

where superscripts "1" and "2" correspond to the terms induced by sources $\boldsymbol{F}_1$ and $\boldsymbol{F}_2$, respectively. Equation (18) is also the basis of the orthogonality relation of Lamb wave mode shapes.

3.3 Orthogonality relation of Lamb wave modes

an infinite single-layer plate of thickness $2d$ as an example, assume the external forces $\boldsymbol{F}_1$ and $\boldsymbol{F}_2$ to be zero, then the two wave fields are two free wave modes. Without losing generality, the two wave fields are assumed as the m^{th} and n^{th} modes. By letting $\boldsymbol{F}_1 = \boldsymbol{F}_2 = 0$ in Equation (18) and integrating it with respect to z, the following condition can be obtained:

$$\frac{1}{r}\frac{\partial}{\partial r}\int_{-d}^{d}\left[r\left(\tilde{v}_r^n \sigma_{rr}^m + v_r^m \tilde{\sigma}_{rr}^n + \tilde{v}_z^n \sigma_{rz}^m + v_z^m \tilde{\sigma}_{rz}^n\right)\right]dz + \left(v_z^m \tilde{\sigma}_{zz}^n + \tilde{v}_z^n \sigma_{zz}^m + v_r^m \tilde{\sigma}_{rz}^n + \tilde{v}_r^n \sigma_{rz}^m\right)\Big|_{-d}^{d} = 0. \tag{19}$$

The plate is not subjected to any external excitations. Thus, it has the traction free boundary condition, that is, $T_{rz}=T_{zz}=0$, on the top ($z=d$) and bottom surface ($z=-d$). Therefore, Equation (19) becomes

$$\frac{\partial}{\partial r}\int_{-d}^{d}\left[r\left(\tilde{v}_r^n \sigma_{rr}^m + v_r^m \tilde{\sigma}_{rr}^n + \tilde{v}_z^n \sigma_{rz}^m + v_z^m \tilde{\sigma}_{rz}^n\right)\right]dz = 0. \tag{20}$$

By substituting Equations (13) and (14) into Equation (20) and changing the integral variable from z to y, the following condition can be obtained:

$$\int_{-d}^{d}\left\{\frac{\partial}{\partial r}r\left[-H_1^{(1)}\left(\xi_n r\right)H_0^{(1)}\left(\xi_m r\right)\left(\overline{v}_x^n\sigma_{xx}^m+v_y^m\overline{\sigma}_{xy}^n\right)\right.\right.$$
$$\left.\left.+H_0^{(1)}\left(\xi_n r\right)H_1^{(1)}\left(\xi_m r\right)\left(v_x^m\overline{\sigma}_{xx}^n+\overline{v}_y^n\sigma_{xy}^m\right)\right]\right\}dy=0 \tag{21}$$

Through derivation, the following condition can be obtained:

$$\int_{-d}^{d}\left\{(\overline{v}_x^n\sigma_{xx}^m+v_y^m\overline{\sigma}_{xy}^n)\left[r\xi_m H_1^{(1)}\left(\xi_n r\right)H_1^{(1)}\left(\xi_m r\right)-r\xi_n H_0^{(1)}(\xi_n r)H_0^{(1)}\left(\xi_m r\right)\right]\right.$$
$$\left.+(v_x^m\overline{\sigma}_{xx}^n+\overline{v}_y^n\sigma_{xy}^m)\left[r\xi_m H_0^{(1)}\left(\xi_n r\right)H_0^{(1)}(\xi_m r)-r\xi_n H_1^{(1)}\left(\xi_n r\right)H_1^{(1)}\left(\xi_m r\right)\right]\right\}dy=0 \tag{22}$$

Without considering material damping, i.e., in the non-leaky plates, both the velocity and stress mode shapes of propagating wave modes are real. Therefore, $\overline{v}_x^n\sigma_{xx}^m+v_y^m\overline{\sigma}_{xy}^n=v_x^m\overline{\sigma}_{xx}^n+\overline{v}_y^n\sigma_{xy}^m$. Equation (22) is thus simplified as

$$\begin{aligned}&\int_{-d}^{d}\left\{(\overline{v}_x^n\sigma_{xx}^m+v_y^m\overline{\sigma}_{xy}^n)\left[r\xi_m H_1^{(1)}\left(\xi_n r\right)H_1^{(1)}\left(\xi_m r\right)-r\xi_n H_0^{(1)}(\xi_n r)H_0^{(1)}\left(\xi_m r\right)\right]\right.\\&\quad\left.+(v_x^m\overline{\sigma}_{xx}^n+\overline{v}_y^n\sigma_{xy}^m)\left[r\xi_m H_0^{(1)}\left(\xi_n r\right)H_0^{(1)}(\xi_m r)-r\xi_n H_1^{(1)}\left(\xi_n r\right)H_1^{(1)}\left(\xi_m r\right)\right]\right\}dy\\&=r\left(\xi_m-\xi_n\right)\left[H_1^{(1)}\left(\xi_n r\right)H_1^{(1)}\left(\xi_m r\right)+H_0^{(1)}(\xi_n r)H_0^{(1)}\left(\xi_m r\right)\right]\int_{-d}^{d}\left\{(\overline{v}_x^n\sigma_{xx}^m+v_y^m\overline{\sigma}_{xy}^n)\right\}dy\\&=0\end{aligned} \tag{23}$$

If $m = n$, the equation is automatically satisfied. If $m \neq n$, then $\int_{-d}^{d}(\overline{v}_x^n\sigma_{xx}^m+v_y^m\overline{\sigma}_{xy}^n)dy=0$ given that $r\left(\xi_m-\xi_n\right)\left[H_1^{(1)}\left(\xi_n r\right)H_1^{(1)}\left(\xi_m r\right)+H_0^{(1)}(\xi_n r)H_0^{(1)}\left(\xi_m r\right)\right]\neq 0$. The orthogonality relation is written as

$$P_{mn}=\int_{-d}^{d}\left(\overline{v}_x^n\sigma_{xx}^m+v_y^m\overline{\sigma}_{xy}^n\right)dy\begin{cases}\neq 0, & \text{if } m=n\\ =0, & \text{if } m\neq n\end{cases} \tag{24}$$

P_{mn} is also the normalization factor in the following derivation of the participation factor.

3.4 Participation factor calculation

Assuming $\boldsymbol{F}_1$ is the PWAS excitation with the angular frequency ω and $\boldsymbol{F}_2$ is zero, then Equation (18) can be simplified as

$$\frac{1}{r}\frac{\partial}{\partial r}\left[r\int_{-d}^{d}\left(\overline{V}_r^2T_{rr}^1+V_r^1\overline{T}_{rr}^2+\overline{V}_z^2T_{rz}^1+V_z^1\overline{T}_{rz}^2\right)dz\right]+\overline{V}_r^2T_{rz}^1\Big|_{-d}^{d}=0. \tag{25}$$

The wave field generated by $\boldsymbol{F}_1$ can be assumed as an expansion of Lamb wave modes as

$$
\begin{aligned}
V_r^1 &= \sum_m a_m(r) v_r^m(z) = i\sum_m a_m(r) v_x^m(y) H_1^{(1)}(\xi_m r) \\
V_z^1 &= \sum_m a_m(r) v_z^m(z) = \sum_m a_m(r) v_y^m(y) H_0^{(1)}(\xi_m r) \\
T_{rr}^1 &= \sum_m a_m(r) \sigma_{xx}^m(y) H_0^{(1)}(\xi_m r) + \sum_m a_m(r) \frac{2\mu}{\omega r} v_x^m(y) H_1^{(1)}(\xi_m r) \\
T_{zz}^1 &= \sum_m a_m(r) \sigma_{yy}^m(y) H_0^{(1)}(\xi_m r) \\
T_{rz}^1 &= \sum_m a_m(r) \sigma_{rz}^m(z) = i\sum_m a_m(r) \sigma_{xy}^m(y) H_1^{(1)}(\xi_m r)
\end{aligned}
\tag{26}
$$

The wave field generated by $\boldsymbol{F}_2$=0 is a free condition, that is, the n^{th} Lamb wave mode that comprises incoming and outgoing components. The second-kind Hankel functions $H_0^{(2)}$ (order 0) and $H_1^{(2)}$ (order 1) indicate the incoming component of Lamb waves with the time dependency term being $e^{-i\omega t}$, as compared with the outgoing waves indicated by first-kind Hankel functions $H_0^{(1)}$ and $H_1^{(1)}$. With the relation between Hankel and Bessel functions given by

$$
\begin{aligned}
H_0^{(1)}(\xi_n r) + H_0^{(2)}(\xi_n r) &= 2J_0(\xi_n r) \\
H_1^{(1)}(\xi_n r) + H_1^{(2)}(\xi_n r) &= 2J_1(\xi_n r)
\end{aligned}
\tag{27}
$$

where $J_0(\xi_n r)$ and $J_1(\xi_n r)$ are respectively the Bessel functions of orders 0 and 1, the wave field can be expressed as:

$$
\begin{aligned}
V_r^2 &= iv_x^n(y)\left[H_1^{(1)}(\xi_n r) + H_1^{(2)}(\xi_n r)\right] = 2iv_x^n(y) J_1(\xi_n r) \\
V_z^2 &= v_y^n(y)\left[H_0^{(1)}(\xi_n r) + H_0^{(2)}(\xi_n r)\right] = 2v_y^n(y) J_0(\xi_n r) \\
T_{rr}^2 &= \sigma_{xx}^n(y)\left[H_0^{(1)}(\xi_n r) + H_0^{(2)}(\xi_n r)\right] + \frac{2\mu}{\omega r} v_x^n(y)\left[H_1^{(1)}(\xi_n r) + H_1^{(2)}(\xi_n r)\right] \\
&\quad = 2\sigma_{xx}^n(y) J_0(\xi_n r) + 2\frac{2\mu}{\omega r} v_x^n(y) J_1(\xi_n r) \\
T_{zz}^2 &= \sigma_{yy}^n(y)\left[H_0^{(1)}(\xi_n r) + H_0^{(2)}(\xi_n r)\right] = 2\sigma_{yy}^n(y) J_0(\xi_n r) \\
T_{rz}^2 &= i\sigma_{xy}^n(y)\left[H_1^{(1)}(\xi_n r) + H_1^{(2)}(\xi_n r)\right] = 2i\sigma_{xy}^n(y) J_1(\xi_n r)
\end{aligned}
\tag{28}
$$

Notably, superscripts "1" and "2" in the left hand side of Equations (26) and (28) represent the responses to the forces $\boldsymbol{F}_1$ and $\boldsymbol{F}_2$, respectively. By substituting Equations (26) and (28) into Equation (25), the following condition can be obtained:

$$
\begin{aligned}
&\frac{1}{r}\frac{\partial}{\partial r}\left\{ r\sum_m a_m(r) \int_{-d}^{d}\left[-J_1(\xi_n r) H_0^{(1)}(\xi_m r)\left(\overline{v_x^n}\sigma_{xx}^m + v_y^m \overline{\sigma_{xy}^n}\right)\right.\right. \\
&\left.\left. \quad + J_0(\xi_n r) H_1^{(1)}(\xi_m r)\left(v_x^m \overline{\sigma_{xx}^n} + \overline{v_y^n}\sigma_{xy}^m\right)\right] dy \right\} = \overline{v_x^n} J_1(\xi_n r) T_{rz}^1(d)
\end{aligned}
\tag{29}
$$

By recalling the orthogonality relation in Equation (24), Equation (29) becomes

$$\frac{P_{nn}}{r}\frac{\partial}{\partial r}\left\{ra_n(r)\left[J_0(\xi_n r)H_1^{(1)}(\xi_n r)-J_1(\xi_n r)H_0^{(1)}(\xi_n r)\right]\right\}=\overline{v}_x^n J_1(\xi_n r)T_{rz}^1(d). \tag{30}$$

The differentiation property of Hankel and Bessel functions provides

$$\frac{\partial}{\partial r}\left\{r\left[J_0(\xi_n r)H_1^{(1)}(\xi_n r)-J_1(\xi_n r)H_0^{(1)}(\xi_n r)\right]\right\}=0. \tag{31}$$

Therefore, Equation (30) is further simplified as

$$P_{nn}\left[J_0(\xi_n r)H_1^{(1)}(\xi_m r)-J_1(\xi_n r)H_0^{(1)}(\xi_n r)\right]\frac{\partial}{\partial r}a_n(\xi_n,r)=\overline{v}_x^n J_1(\xi_n r)T_{rz}^1(d). \tag{32}$$

By substituting the PWAS excitation given in Equations (3) and (4) into Equation (32) and conducting integration, the final expression of the participation factor is

$$a_n(\xi_n,r)=\frac{\overline{v}_x^n J_1(\xi_n a)a\tau_a}{P_{nn}\left[J_0(\xi_n a)H_1^{(1)}(\xi_n a)-J_1(\xi_n a)H_0^{(1)}(\xi_n a)\right]}. \tag{33}$$

Equation (33) indicates that a_n is a function of the wavenumber and is independent of the distance from the sensor. Therefore, the in-plane displacement and strain of the n^{th} wave packet are

$$\begin{aligned}U_r^n(r)&=i\frac{\overline{v}_x^n J_1(\xi_n a)a\tau_a}{P_{nn}\left[J_0(\xi_n a)H_1^{(1)}(\xi_n a)-J_1(\xi_n a)H_0^{(1)}(\xi_n a)\right]}u_x^n H_1^{(1)}(\xi_n r)\\ \varepsilon_r^n(r)&=i\frac{\overline{v}_x^n J_1(\xi_n a)a\tau_a}{P_{nn}\left[J_0(\xi_n a)H_1^{(1)}(\xi_n a)-J_1(\xi_n a)H_0^{(1)}(\xi_n a)\right]}u_x^n\left[\xi_n H_0^{(1)}(\xi_n r)-\frac{H_1^{(1)}(\xi_n r)}{r}\right]\end{aligned}. \tag{34}$$

The out-of-plane displacement of the n^{th} wave packet is

$$U_z^n(r)=\frac{\overline{v}_x^n J_1(\xi_n a)a\tau_a}{P_{nn}\left[J_0(\xi_n a)H_1^{(1)}(\xi_n a)-J_1(\xi_n a)H_0^{(1)}(\xi_n a)\right]}u_y^n H_0^{(1)}(\xi_n r). \tag{35}$$

The corresponding out of plane velocity of the n^{th} wave packet is

$$V_z^n(r)=-i\omega U_z^n(r)=\frac{-i\omega\overline{v}_x^n J_1(\xi_n a)a\tau_a}{P_{nn}\left[J_0(\xi_n a)H_1^{(1)}(\xi_n a)-J_1(\xi_n a)H_0^{(1)}(\xi_n a)\right]}u_y^n H_0^{(1)}(\xi_n r). \tag{36}$$

Equations (34) through (36) actually indicate that the Hankel functions account for the decrease in amplitude induced by the geometric spreading and are the tuning curves of the corresponding responses. In the derivations in this section, the mode shapes and the normalization factor impose no limitations on the plate thickness variation and the direction dependency is not considered. Therefore, the multi-layer plate is isotropic within each layer. The present derivation is applicable to multi-layer isotropic plates.

It should also be noted that, according to the differentiation property of Hankel functions given in Equation (31), the response to any kind of external excitations, in addition to PWAS excitation, can be obtained as

$$\begin{aligned}\frac{1}{r}\frac{\partial}{\partial r}\int_{-d}^{d}\left[r\left(\bar{V}_r^2 T_{rr}^1+V_r^1\bar{T}_{rr}^2+\bar{V}_z^2 T_{rz}^1+V_z^1\bar{T}_{rz}^2\right)\right]dz=-\int_{-d}^{d}\left[-2i\bar{v}_x^n J_1(\xi_n r)F_r^1+2\bar{v}_y^n J_0(\xi_n r)F_z^1\right]dz\\ -\left[V_z^1\bar{\sigma}_{yy}^n J_0(\xi_n r)+\bar{v}_y^n J_0(\xi_n r)T_{zz}^1-iV_r^1\bar{\sigma}_{xy}^n J_1(\xi_n r)-i\bar{v}_x^n J_1(\xi_n r)T_{rz}^1\right]\Big|_{-d}^{d}\end{aligned} \quad . \quad (37)$$

The left hand side of Equation (37) is the same as that in Equation (32). Therefore, the complete expression of the participation factor is

$$\begin{aligned}a_n(\xi_n,r)=\int_0^r\Bigg\{&\frac{-\int_{-d}^{d}\left(-2i\bar{v}_x^n J_1(\xi_n r)F_r^1+2\bar{v}_y^n J_0(\xi_n r)F_z^1\right)dz}{P_{nn}\left[J_0(\xi_n r)H_1^{(1)}(\xi_n r)-J_1(\xi_n r)H_0^{(1)}(\xi_n r)\right]}\\ &\frac{-\left[V_z^1\bar{\sigma}_{yy}^n J_0(\xi_n r)+\bar{v}_y^n J_0(\xi_n r)T_{zz}^1-iV_r^1\bar{\sigma}_{xy}^n J_1(\xi_n r)-i\bar{v}_x^n J_1(\xi_n r)T_{rz}^1\right]\Big|_{-d}^{d}}{P_{nn}\left[J_0(\xi_n r)H_1^{(1)}(\xi_n r)-J_1(\xi_n r)H_0^{(1)}(\xi_n r)\right]}\Bigg\}dr\end{aligned} \quad . \quad (38)$$

Equation (38) applies to any kind of direction independent external loads.

In the ITM, the transforms of the plate wave governing equations shown in Equations (9) and (10) are conducted first and then the solutions in the wavenumber frequency domain are transferred back to the time domain. Therefore, a set of governing equations of the plate waves is required. For multi-layer plates, such equations are unavailable and the ITM is thus inapplicable. On the contrary, as shown in Equation (38), not only various external excitations can be considered, but body forces F_r and F_z, excitation induced stresses T_{zz} and T_{rz}, and the material variation in the thickness direction can also be accounted in the corresponding mode shapes. Therefore, the NME method applies to multi-layer plates as well.

3.5 Wave field calculation

The modal participation factor calculated above is a function of the excitation frequency applied on the PWAS. Therefore, this factor is related to the transfer function of the PWAS-plate system. In practice, a short period excitation, such as tone bursts, contains broad frequency components. The response frequency spectrum is obtained by multiplying the frequency spectrum of the excitation by the transfer function of the corresponding response.

The time domain responses are calculated by the inverse Fourier transform. The flowchart of the entire process is given in Figure 3.

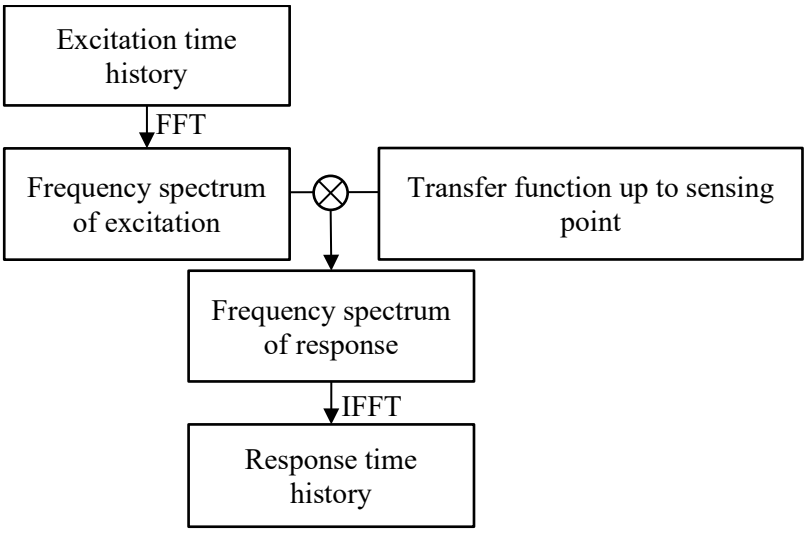

Figure 3 Flowchart of wave field calculation

4 Wave field in single-layer isotropic plates

The proposed NME method is applied to single-layer isotropic plates to calculate the tuning curves and the wave field in this section.

4.1 Tuning curves of single-layer plates

An infinite T2024-3 aluminum plate of 2.032 mm thickness is studied here. The material properties are given in Table 1. A circular PWAS of 7 mm diameter and 0.5 mm thickness is attached on the surface of the plate. The perfect bonding between the PWAS and the plate is assumed. Thus, the pin-force model described in Section 2 is used. The excitation voltage is 10 V peak to peak, and the piezoelectric coefficient is $d_{31} = -190$ V/m.

Table 1 Material properties

Material	Parameter	Unit	Value
Aluminum	Density	kg/m^3	2780
	Young's Modulus	GPa	73.1
	Poisson's ratio	—	0.33
Steel	Density	kg/m^3	7850
	Young's Modulus	GPa	206
	Poisson's ratio	—	0.3
Epoxy	Density	kg/m^3	1000
	Young's Modulus	GPa	3.5
	Poisson's ratio	—	0.38

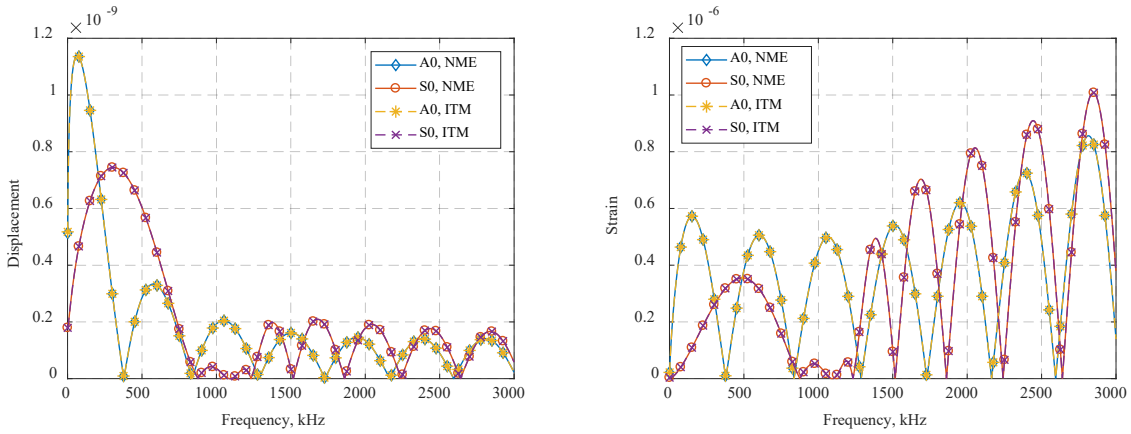

(a)Tuning curve of in-plane displacement U_r (b) Tuning curve of in-plane strain ε_r

Figure 4 Tuning curves of the aluminum plate

The tuning curves of the in-plane displacement U_r and strain ε_r of the plate are obtained using the proposed NME method. The first antisymmetric (A0) mode and symmetric (S0) mode tuning curves obtained at 50 mm away from the PWAS center, which are compared with their counterparts obtained with the ITM, are shown in Figure 4. The two curves obtained with the two methods are nearly the same, which verifies the accuracy of the proposed NME method. The A0 and S0 modes show different fluctuation patterns. Both modes increase rapidly first with the increase in frequency increase, with A0 mode peaking at 65 kHz and S0 peaking at 309 kHz, at which A0 mode nearly disappears. In fact, the tuning curve for A0 mode is nearly zero at 379 kHz, and this condition indicates that the A0 is "rejected" at this excitation frequency. By taking the advantages of the distribution of nodes of A0 and S0 modes, proper excitation frequencies can be chosen to tune the desired wave modes in practice for given

PWAS. Equation (34) shows that the term $J_1(\xi_n a)$ determines the nodes in the tuning curves. Therefore, the tuning curves can also be used to determine the dimension of the PWAS for obtaining the optimal response at desired excitation frequencies.

4.2 Wave field calculation

The wave field in the aluminum plate with the surface-mounted PWAS is calculated using the NME method. A three-count Hanning-windowed tone burst excitation of a 90 kHz center frequency and a 10 V peak-to-peak amplitude is applied on the PWAS. The excitation wave form and corresponding frequency spectrum are shown in Figure 5. The A0 and S0 mode tuning curves of the out-of-plane velocity at 50 mm away from the PWAS center are obtained and plotted in Figure 6. The time domain signal is calculated through the inverse Fourier transform of the product of the transfer function and the excitation frequency spectrum.

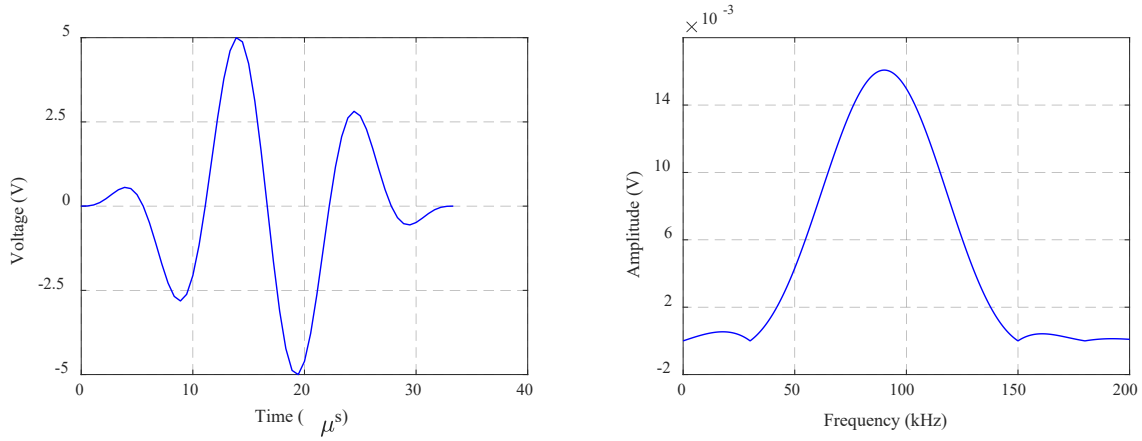

(a) Excitation wave form (b) Frequency spectrum

Figure 5 Excitation wave

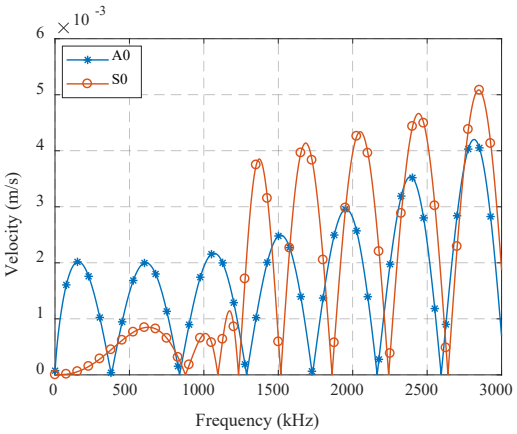

Figure 6 Tuning curve of out-of-plane velocity

The wave fields of the plate are also calculated using commercial finite element analysis (FEA) software Abaqus[32]. As the FEA cannot simulate an infinite physical region, an aluminum plate of 140 mm×140 mm×2.032 mm is studied. A total of 30 sets of damper elements are applied to the peripheral region of the plate, covering 30 mm from the borders, to eliminate the reflections on the plate boundary and simulate the "infinite" plate (Figure 7). The damper elements are set in the normal direction and two shear directions with linearly increasing damping ratios[33] to absorb the normal and shear stress waves, as shown in Figure 7(b). The plate material and PWAS are the same as those in the theoretical calculation. The bottom surface of the PWAS is coupled to the plate with the "Tie" constraint type, such that all six degrees of freedom of the nodes in the interface are identical. The C3D8E coupled field elements are chosen for the PWAS and C3D8R elements for the plate. The maximum mesh size of the PWAS is 0.5 mm and the plate is discretized as 1 mm×1 mm×0.508 mm to meet the convergence and accuracy requirements. The element size is smaller than 1/20 of the wave length, which is approximately 44 mm at the frequency of 180 kHz (double the center frequency).

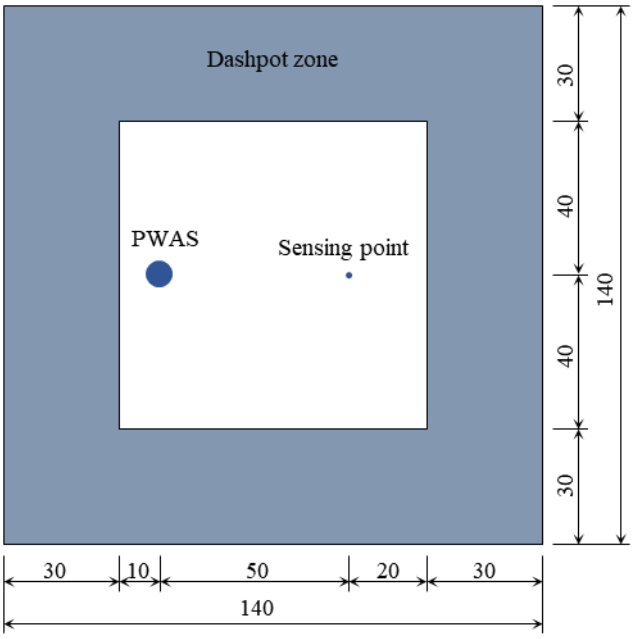

(a) FEA model schematic

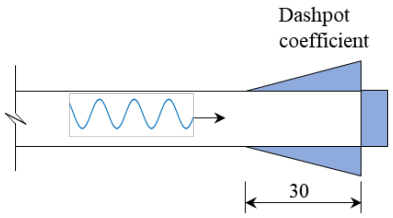

(b) Dashpot coefficient variation (cross section view)

Figure 7 FEA model and dashpot coeeficient variation (Unit: mm)

The dashpot coefficients are determined by

$$c_N = \frac{a}{4}(S_1 + S_2 + S_3 + S_4)\rho c_P$$
$$c_T = \frac{b}{4}(S_1 + S_2 + S_3 + S_4)\rho c_S \tag{39}$$

where S_1 to S_4 are areas of the four elements around the joint where the dashpot is applied; and a and b are the viscous coefficients for the normal and shear stresses, respectively[34].

The same voltage excitation shown in Figure 5 is applied on the top surface of the PWAS, and the bottom surface of the PWAS is grounded. After the implicit dynamic analysis, the out-of-plane velocities are extracted. The wave fields of the plate at 10 and 40 μs are displayed in Figure 8. Figure 8(b) shows that the boundary reflections are effectively absorbed by the dashpots and that only small reflections are retained.

The sensing point is located 50 mm away from the PWAS transmitter center. The normalized velocity at this point obtained using the proposed NME method is compared with the FEA result in Figure 9. At this point, the S0 and A0 wave packets intersect with each other and form one large wave packet. In particular, the S0 wave packet fluctuates in a small amplitude,

whereas the A0 wave packet fluctuates in a large amplitude. This result is expected from the tuning curves in Figure 6, in which the A0 mode amplitude is around 100 times the S0 mode amplitude at 90 kHz. The two sets of results match well for the direct incident waves except that the FEA results have some reflections from the plate boundaries after 60 μs. Therefore, the proposed NME method can calculate the wave field in a single-layer plate accurately.

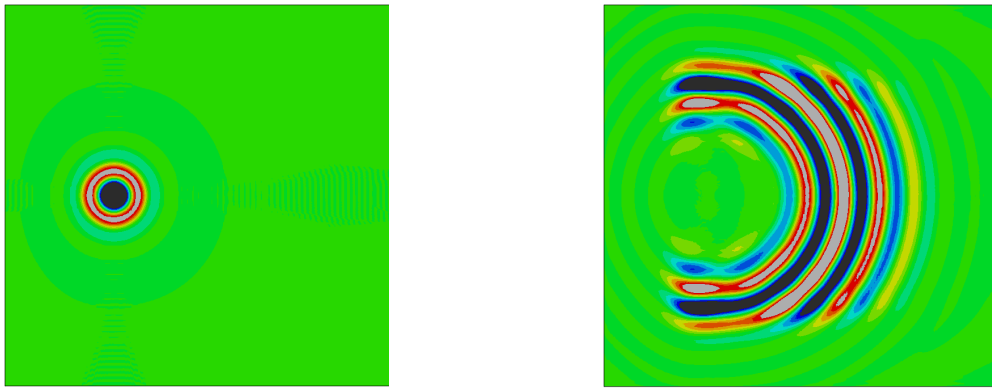

(a) Out-of-plane velocity field at 10 μs (b) Out-of-plane velocity field at 40 μs

Figure 8 Out-of-plane velocity field

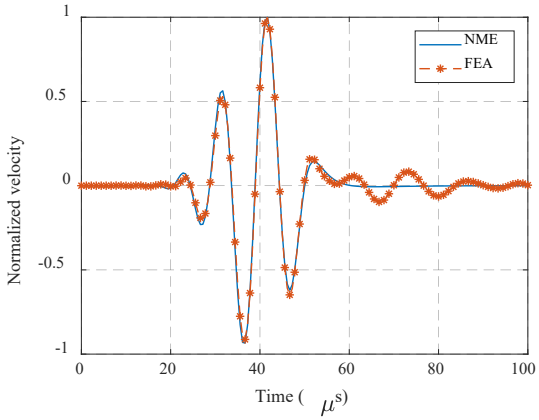

Figure 9 Normalized out-of-plane velocity at sensing point in a single-layer plate

4.3 Experimental validation

An experimental study is carried out to further validate the theoretical calculation. The experimental setup is illustrated in Figure 10. The aluminum plate is 2.032 mm thick and has a plan dimension of 700 mm×700 mm. The plate material properties are the same as listed in Table 1. The surface-bonded PWAS (Steminc SM412) is 7 mm in diameter and 0.5 mm in

thickness. Near the border of the aluminum plate, a layer of clay (NSP non-drying modeling clay) as shown in Figure 10(b) and (c) is attached on both surfaces of the plate to absorb the stress waves and eliminate the reflections from the plate borders, as an approximation of the "infinite" plate configuration. The clay strips are around 50 mm wide. The excitation wave shown in Figure 5(a) was generated by the Tektronics AFG3052C dual channel function generator, then amplified to 140 V peak to peak by the NF HAS4014 high-speed bipolar amplifier and applied on the PWAS. The out-of-plane velocities at the two sensing points located 50 mm (sensing point 1) and 100 mm (sensing point 2) away from the PWAS center were measured using the Polytec PSV-400 scanning laser doppler vibrometer (LDV) at a sampling frequency of 50 MHz.

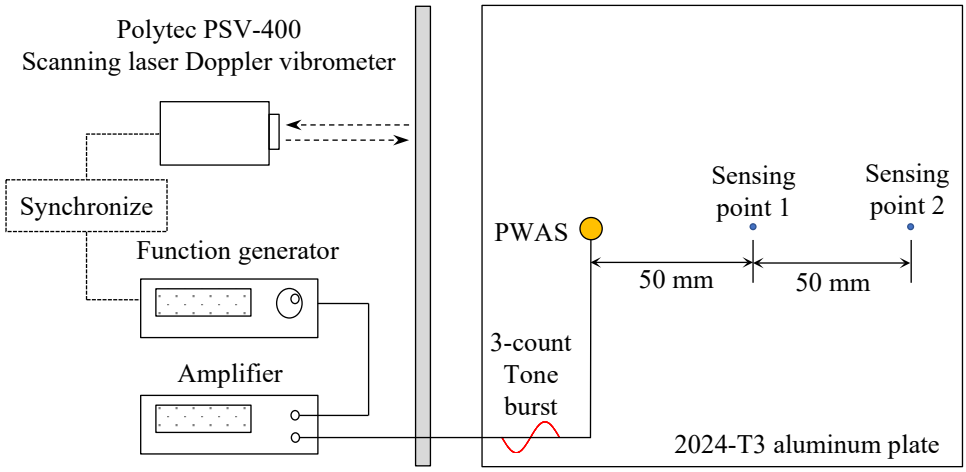

(a) Schematic configuration

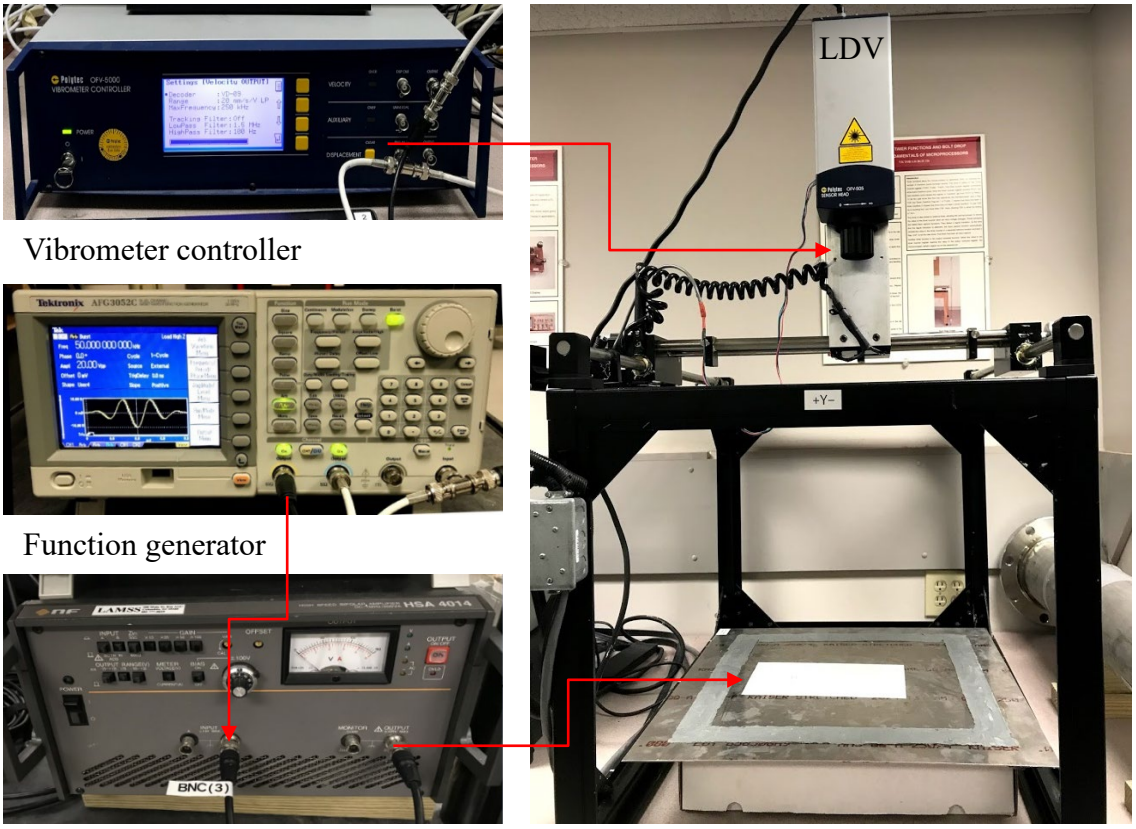

(b) Physical experimental setup

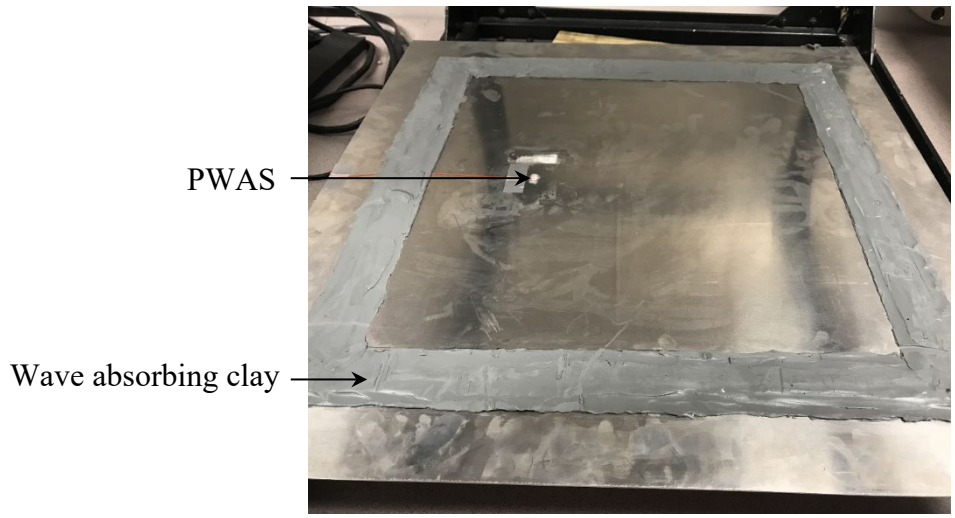

(c) Aluminum plate with wave absorbing clay

Figure 10 Experimental setup

The normalized out-of-plane velocity obtained in the experiment and the NME calculations are compared in Figure 11. The normalization factors of the experimental and the NME calculation

results are their corresponding maximum absolute velocity at sensing point 1. In each of the four lines in the figure, one wave packet merged by the S0 and A0 wave packets is observed. The wave packet amplitude at sensing point 2 is around 70% of that at sensing point 1, which is due to the geometric spreading and revealed by the Hankel function term $H_0^{(1)}(\xi_n r)$ in Equation (36). Meanwhile, the wave packet of sensing point 2 has a longer duration than that of sensing point 1, which is a reflection of the dispersive nature of the Lamb waves. The wave propagation time and packet shapes obtained using NME method are in excellent agreement with the corresponding experimental results, except that the boundary reflections appear at around 140 μs in the experiment results, whereas the NME prediction considers only the direct incident waves.

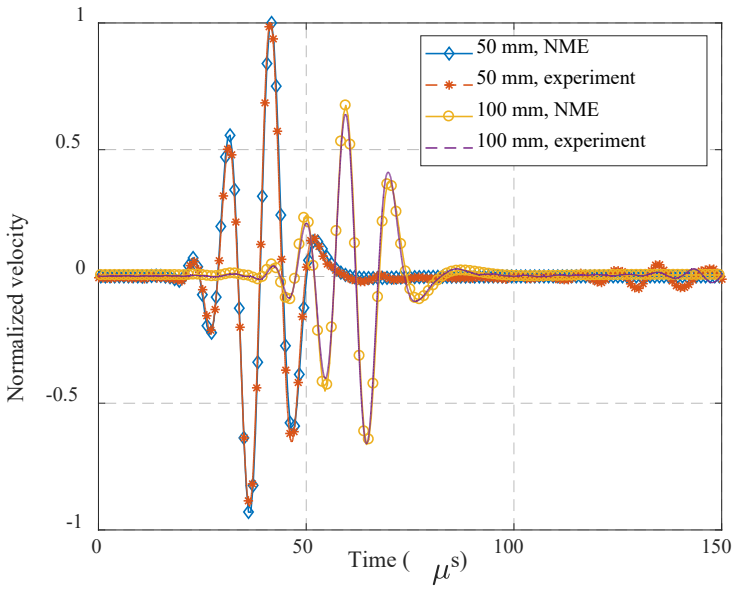

Figure 11 Out-of-plane velocities

5 Wave field in multi-layer isotropic plates

As discussed above, the assumption adopted in the NME derivations imposes limitations on the direction dependency but no limitation on material variations in the thickness direction. Therefore, this method is also applicable to multi-layer plates made of isotropic materials. In fact, the single-layer plate model can be treated as a multi-layer plate made of identical materials in each layer. In the case, the tuning curves and time history results obtained using

the multi-layer model are exactly the same as those obtained with the single-layer model. The results are not presented here for the sake of conciseness. For multi-layer application, a triple-layer plate made of different materials is studied in this section.

5.1 Tuning curves at sensing point in a double-layer plate

The triple-layer plate is made of a T-2023 aluminum layer (1 mm thickness) and a 304 stainless steel layer (1 mm thickness), with an 0.2 mm thick adhesive film sandwiched in between. The adhesive layer is assumed to guarantee the perfect bonding at both interfaces. The material properties are also listed in Table 1. The same PWAS configurations are adopted with same excitation applied on it. The wavenumber and group velocity dispersion curves are first calculated using GMM, and the corresponding stress and velocity mode shapes are shown in Figure 12(a) and (b). The velocity and stress mode shapes in the multi-layer plate lost the symmetry or anti-symmetry nature present in the single-layer aluminum plate. The interface traction and displacement continuity imposed by Equation (15) is guaranteed and the traction-free surface boundary conditions (T_{rz}=T_{zz}=0) are valid in the figures. At the same time, the continuity of T_{rr} at the interface does not exist because this component is internally balanced and does not interact with the adjacent layer. Based on these mode shapes, the out-of-plane velocity tuning curves of the triple-layer plates at 0.05 m away from the PWAS center are presented in Figure 13. In Figure 13, the first mode has a much lower amplitude at frequencies lower than 500 kHz, which means at excitation in such frequency range, the first wave packet time history should have a smaller amplitude as well, as will be shown in next section.

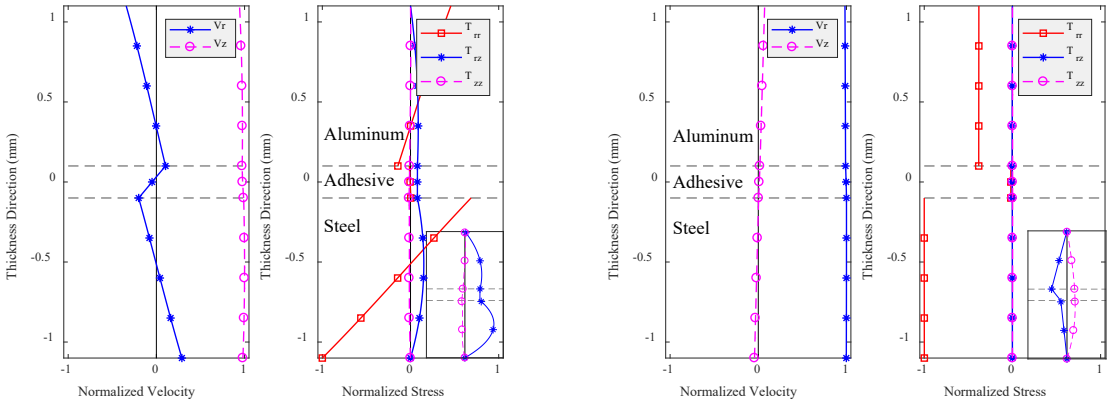

(a) Normalized velocity and stress mode shapes of 1st mode

(b) Normalized velocity and stress mode shapes of 2nd mode

Figure 12 Velocity and stress mode shapes of the first two modes of the aluminum-adhesive-

steel plate

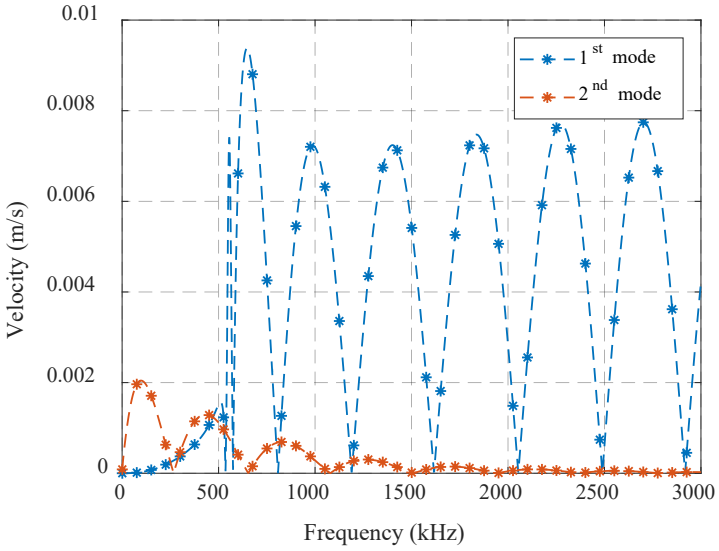

Figure 13 Tuning curves of out-of-plane velocity in the aluminum-adhesive-steel plate

5.2 Wave field in the multi-layer plate

The wave field of the plate is calculated by performing the inverse Fourier transform of the product of the transfer function and the excitation frequency spectrum. The results are then compared with the FEA counterparts.

The FEA model of the aluminum-adhesive-steel triple-layer plate is built in a similar way as that in Section 4.2, with the material properties listed in Table 1. The normalized out-of-plane velocities obtained using the NME method and the FEA are plotted in Figure 14. In Figure 14(a), the separated wave packets of the first two modes at 50 mm away from the PWAS center are presented. As stated earlier, the amplitude of the first mode is much lower than that of the second one. Due to the short travel distance, the two wave packets merged into one which is directly obtained in the FEA results as shown in Figure 14(b). The normalized out-of-plane velocities at 50 mm and 100 mm away match well with those analytical results obtained with NME in terms of both the wave traveling time and wave packet shape.

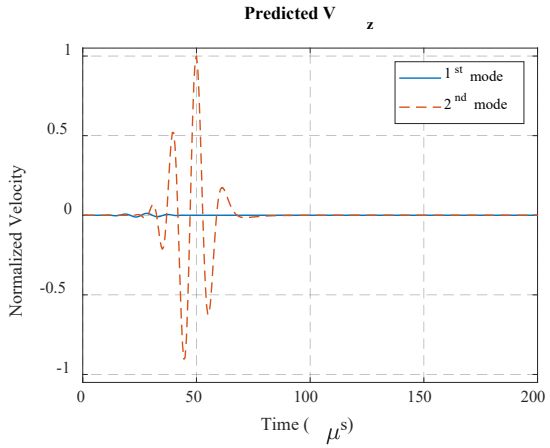

(a) Separated wave packets of the first two wave modes obained with NME

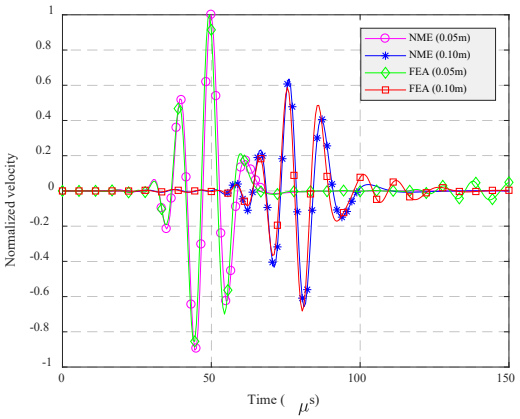

(b) Normalized out-of-plane velociy

Figure 14 Normalized out-of-plane velocity in the aluminum-adhesive-steel triple-layer plate

5.3 Experimental validation

An experimental study with a similar aluminum-adhesive-steel plate is carried out to validate the theoretical calculation. The overall experimental setup is similar to those shown in Figure 10, while the aluminum-adhesive-steel triple layer plate shown in Figure 15. The plate material properties are the same as listed in Table 1. The PWAS attachment and voltage excitation are the same as those in the previous experiment in Section 4.3. The out-of-plane velocities at 50 mm and 100 mm away were measured. The normalized results are shown in Figure 16. Excellent agreement between the NME calculation and the experiment are obtained in terms of travelling time and wave packet shapes, indicating the proposed NME method is applicable to the Lamb wave field calculation in multi-layer isotropic plates as well as in single-layer isotropic plates.

(a) Aluminum-adhesive-steel plate

(b) Plate thickness zoom-in view

Figure 15 Aluminum-adhesive-steel plate configuration

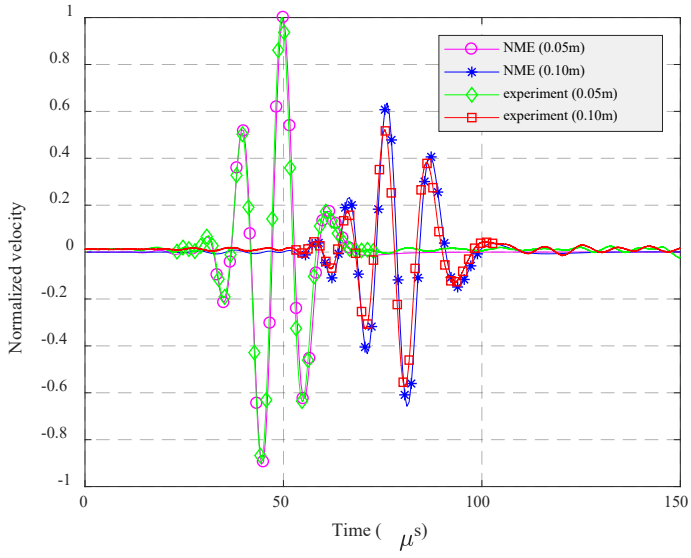

Figure 16 Out-of-plane velocities

6 Conclusion and discussion

In this study, the NME method is developed to calculate the wave field in single- and multi-layer isotropic plates generated by a surface-mounted PWAS excitation. The orthogonality nature of the Lamb wave modes enables the calculation of the participation factor of each Lamb wave mode and consequently the desired tuning curves are obtained with the NME method. The tuning curves of a single-layer plate obtained from the proposed NME method are consistent with the ITM results. The time domain responses are in excellent agreement with the FEA and experiments, in which damper elements and clay are respectively used to absorb the boundary reflections. The NME method is applied to an aluminum-adhesive-steel triple layer plate and the analytical out-of-plane velocity are similar to those of FEA and experiments.

This study established the theoretical basis of the circular crested Lamb wave fields in multi-layer plates in the healthy state and can facilitate the further studies of the wave fields in the damaged state. In fact, the formulae derived in this paper can x be directly applied to the general Lamb wave field calculation in multi-layer isotropic plates with the consistent bonding condition at the interface, not necessarily to be perfect bonding. For example, the Lamb wave

field in a multi-layer plate with the overall imperfect bonding condition, in which the interface tractions are matched while the interface displacements are not necessarily continuous (i.e., the bond-slip model), can be calculated following the exactly same procedures in the present paper after the interface traction and displacement condition are updated. Other local damages such as dents and cracks, which introduce scattering wave packages, can be detected and located by the separated scattering waves obtained by subtracting the pristine wave field output from the total output of the structural health monitoring system. Further studies will focus on the scattering properties of different types of damages alone with the results presented in this study.

It should also be noted that direction independency is considered in the derivations in this study, therefore the formulae can be applied to multi-layer isotropic plates (for example metal plates) or quasi-isotropic plates (for example fiber-reinforced polymer multi-layer plates with different lamination angles and woven composite plate) subject to axisymmetric loadings. In a plate made of generally anisotropic layers, or when the excitation is not axisymmetric, the direction dependency should be accounted. Future studies will focus on the direction dependency in generally anisotropic multi-layer plates subjected to generally external excitations following the procedures presented in this paper. The wave fields of general anisotropic plates merit further development in the future.

7 Acknowledgement

This research was supported by The Hong Kong Polytechnic University Research Grant (No. 1-BBAG) and the RGC Theme-based Research Scheme (Project No. T22-502/18-R). The first author is grateful to the Research Grants Council of the Hong Kong Special Administrative Region for the Hong Kong PhD Fellowship Award.

8 References

[1] Su, Z., Ye, L. and Lu, Y., Guided Lamb waves for identification of damage in composite structures: A review. *Journal of Sound and Vibration*, 2006. **295**(3-5): p. 753-780.

[2] Alers, G.A., Burns Jr, L.R. and MacLauchlan, D.T., Electromagnetic acoustic transducer. 1988, Google Patents.

[3] Wilcox, P.D., Omni-directional guided wave transducer arrays for the rapid inspection of large areas of plate structures. *IEEE transactions on ultrasonics, ferroelectrics, and frequency control*, 2003. **50**(6): p. 699-709.

[4] Yu, L. and Giurgiutiu, V., In situ 2-D piezoelectric wafer active sensors arrays for guided wave damage detection. *Ultrasonics*, 2008. **48**(2): p. 117-134.

[5] Meitzler, A., Tiersten, H., Warner, A., Berlincourt, D., Couqin, G. and Welsh III, F., IEEE standard on piezoelectricity. 1988.

[6] Giurgiutiu, V., Structural Health Monitoring with Piezoelectric Wafer Active Sensors: with Piezoelectric Wafer Active Sensors. 2007: Elsevier.

[7] Shen, Y. and Giurgiutiu, V., Predictive modeling of nonlinear wave propagation for structural health monitoring with piezoelectric wafer active sensors. *Journal of Intelligent Material Systems and Structures*, 2013. **25**(4): p. 506-520.

[8] Shen, Y. and Giurgiutiu, V., Combined analytical FEM approach for efficient simulation of Lamb wave damage detection. *Ultrasonics*, 2016. **69**: p. 116-28.

[9] Lowe, M.J., Matrix techniques for modeling ultrasonic waves in multilayered media. *IEEE transactions on ultrasonics, ferroelectrics, and frequency control*, 1995. **42**(4): p. 525-542.

[10] Knopoff, L., A matrix method for elastic wave problems. *Bulletin of the Seismological Society of America*, 1964. **54**(1): p. 431-438.

[11] Rose, J.L., Ultrasonic guided waves in solid media. 2014: Cambridge university press.

[12] Wang, L. and Rokhlin, S.I., Stable reformulation of transfer matrix method for wave propagation in layered anisotropic media. *Ultrasonics*, 2001. **39**(6): p. 413-424.

[13] Leckey, C.A., Rogge, M.D. and Parker, F.R., Guided waves in anisotropic and quasi-isotropic aerospace composites: Three-dimensional simulation and experiment. *Ultrasonics*, 2014. **54**(1): p. 385-394.

[14] Gopalakrishnan, S., Ruzzene, M. and Hanagud, S., Spectral finite element method, in *Computational Techniques for Structural Health Monitoring*. 2011, Springer. p. 177-217.

[15] Loveday, P.W., Semi-analytical finite element analysis of elastic waveguides subjected to axial loads. *Ultrasonics*, 2009. **49**(3): p. 298-300.

[16] Velichko, A. and Wilcox, P.D., Modeling the excitation of guided waves in generally anisotropic multilayered media. *The Journal of the Acoustical Society of America*, 2007. **121**(1): p. 60-69.

[17] Bai, H., Zhu, J., Shah, A. and Popplewell, N., Three-dimensional steady state Green function for a layered isotropic plate. *Journal of Sound and Vibration*, 2004. **269**(1-2): p. 251-271.

[18] Giurgiutiu, V., Tuned Lamb wave excitation and detection with piezoelectric wafer active sensors for structural health monitoring. *Journal of intelligent material systems and structures*, 2005. **16**(4): p. 291-305.

[19] Santoni-Bottai, G. and Giurgiutiu, V., Exact shear-lag solution for guided waves tuning with piezoelectric-wafer active sensors. *AIAA journal*, 2012. **50**(11): p. 2285-2294.

[20] Shen, Y. and Giurgiutiu, V., WaveFormRevealer: An analytical framework and predictive

tool for the simulation of multi-modal guided wave propagation and interaction with damage. *Structural Health Monitoring*, 2014. **13**(5): p. 491-511.
[21] Liu, G.-R. and Xi, Z., Elastic waves in anisotropic laminates. 2001: CRC press.
[22] Barouni, A.K. and Saravanos, D.A., A layerwise semi-analytical method for modeling guided wave propagation in laminated and sandwich composite strips with induced surface excitation. *Aerospace Science and Technology*, 2016. **51**: p. 118-141.
[23] Achenbach, J. and Xu, Y., Wave motion in an isotropic elastic layer generated by a time-harmonic point load of arbitrary direction. *The Journal of the Acoustical Society of America*, 1999. **106**(1): p. 83-90.
[24] Kamal, A.M., Lin, B. and Giurgiutiu, V., Exact analytical modeling of power and energy for multimode lamb waves excited by piezoelectric wafer active sensors. *Journal of intelligent material systems and structures*, 2014. **25**(4): p. 452-471.
[25] Weaver, R. and Pao, Y.-H., Axisymmetric elastic waves excited by a point source in a plate. *Journal of Applied Mechanics*, 1982. **49**(4): p. 821-836.
[26] Moulin, E., Assaad, J., Delebarre, C. and Osmont, D., Modeling of Lamb waves generated by integrated transducers in composite plates using a coupled finite element–normal modes expansion method. *The Journal of the Acoustical Society of America*, 2000. **107**(1): p. 87-94.
[27] Santoni, G., Fundamental studies in the Lamb-wave interaction between piezoelectric wafer active sensor and host structure during structural health monitoring. 2010, University of South Carolina.
[28] Mei, H. and Giurgiutiu, V., Guided wave excitation and propagation in damped composite plates. *Structural Health Monitoring*, 2018: p. 1475921718765955.
[29] Achenbach, J. and Achenbach, J., Reciprocity in elastodynamics. 2003: Cambridge University Press.
[30] Graff, K.F., Wave motion in elastic solids. 2012: Courier Corporation.
[31] Auld, B.A., Acoustic fields and waves in solids. Vol. II. 1990, Malabar, FL: Krieger Publishing Company.
[32] Dassault Systèmes Simulia Corp, Abaqus Theory Manual (6.12). *Dassault Systemes Simulia Corp., Providence, RI, Last accessed Nov*, 2013. **9**: p. 2013.
[33] Shen, Y. and Giurgiutiu, V., Effective non-reflective boundary for Lamb waves: Theory, finite element implementation, and applications. *Wave Motion*, 2015. **58**: p. 22-41.
[34] Lysmer, J. and Kuhlemeyer, R.L., Finite dynamic model for infinite media. *Journal of the Engineering Mechanics Division*, 1969. **95**(4): p. 859-878.